nature COMMUNICATIONS

ARTICLE

Received 24 May 2011 | Accepted 27 Oct 2011 | Published 6 Dec 2011

DOI: 10.1038/ncomms1573

Spin waves and magnetic exchange interactions in insulating $Rb_{0.89}Fe_{1.58}Se_2$

Miaoyin Wang[1], Chen Fang[2], Dao-Xin Yao[3], GuoTai Tan[1,4], Leland W. Harriger[1], Yu Song[1], Tucker Netherton[1], Chenglin Zhang[1], Meng Wang[1,5], Matthew B. Stone[6], Wei Tian[7], Jiangping Hu[2,5] & Pengcheng Dai[1,5,6]

The parent compounds of iron pnictide superconductors are bad metals with a collinear antiferromagnetic structure and Néel temperatures below 220 K. Although alkaline iron selenide $A_yFe_{1.6+x}Se_2$ (A = K, Rb, Cs) superconductors are isostructural with iron pnictides, in the vicinity of the undoped limit they are insulators, forming a block antiferromagnetic order and having Néel temperatures of roughly 500 K. Here we show that the spin waves of the insulating antiferromagnet $Rb_{0.89}Fe_{1.58}Se_2$ can be accurately described by a local moment Heisenberg Hamiltonian. A fitting analysis of the spin wave spectra reveals that the next-nearest neighbour couplings in $Rb_{0.89}Fe_{1.58}Se_2$, $(Ba,Ca,Sr)Fe_2As_2$, and $Fe_{1.05}Te$ are of similar magnitude. Our results suggest a common origin for the magnetism of all the Fe-based superconductors, despite having different ground states and antiferromagnetic orderings.

[1] Department of Physics and Astronomy, The University of Tennessee, Knoxville, Tennessee 37996-1200, USA. [2] Department of Physics, Purdue University, West Lafayette, Indiana 47907, USA. [3] State Key Laboratory of Optoelectronic Materials and Technologies, Sun Yat-sen University, Guangzhou 510275, China. [4] College of Nuclear Science and Technology, Beijing Normal University, Beijing 100875, China. [5] Beijing National Laboratory for Condensed Matter Physics and Institute of Physics, Chinese Academy of Sciences, P. O. Box 603, Beijing 100190, China. [6] Neutron Scattering Science Division, Oak Ridge National Laboratory, Oak Ridge, Tennessee 37831-6393, USA. [7] Ames Laboratory and Department of Physics and Astronomy Iowa State University, Ames, Iowa 50011, USA. Correspondence and requests for materials should be addressed to P.D. (email: pdai@utk.edu).

Soon after the discovery of superconductivity in iron pnictides[1], calculations and experiments found that the electronic band structures of these materials are composed of hole and electron Fermi pockets near the Γ(0,0) and M(1,0)/M(0,1) points, respectively[2]. As a consequence, sign-reversed quasiparticle excitations between the hole and electron pockets can induce $s^{\pm}$-wave superconductivity, giving rise to a neutron spin resonance at the in-plane antiferromagnetic (AF) wave vector $Q=(1,0)$ (Fig. 1)[3–7]. These results suggest that the $s^{\pm}$-wave electron pairing mechanism is a leading candidate for the microscopic origin of superconductivity in all iron-based superconductors[2].

The recent discovery of alkaline iron selenide $A\mathrm{Fe}_{1.6+x}\mathrm{Se}_2$ (A = K, Rb, Cs) superconductors[8–12] has generated considerable new excitement in the condensed matter physics community because superconductivity in these materials may have a different origin from the sign-reversed s-wave electron-pairing mechanism[13–16]. Although $A\mathrm{Fe}_{1.6+x}\mathrm{Se}_2$ are isostructural with the metallic AF iron pnictides such as (Ba,Ca,Sr)$\mathrm{Fe}_2\mathrm{As}_2$ (ref. 3), they are insulators near $x=0$ (refs 10–12) and form a $\sqrt{5}\times\sqrt{5}$ block AF structure with Fe vacancy order (Fig. 1a) completely different from the iron pnictides[17–22]. If sign-reversed electron-hole pocket excitations between Γ(0,0) and M(1,0)/M(0,1) points are necessary for superconductivity, superconductivity in alkaline iron selenides should have a different microscopic origin because angle-resolved photoemission experiment measurements on these materials reveal only electron Fermi surfaces at M(1,0)/M(0,1) points and no hole Fermi pockets at Γ(0,0) point[13–15]. On the other hand, if AF spin excitations are responsible for superconductivity in Fe-based superconductors[23], one would expect that spin waves in the parent compounds of different classes of Fe-based superconductors have a similar energy scale despite dramatically different transport and magnetic properties. Previous work on spin waves of (Ba,Ca,Sr)$\mathrm{Fe}_2\mathrm{As}_2$ (refs 24–26) and $\mathrm{Fe}_{1.05}\mathrm{Te}$ (ref. 27) suggests that the overall magnetic spectra can only be described by considering both the local and itinerant electrons, and the next-nearest neighbour (NNN) exchange couplings in these materials are similar. Because the insulating $A\mathrm{Fe}_{1.6+x}\mathrm{Se}_2$ has completely different magnetic structure, Néel temperatures, and static-ordered moments (Fig. 1) from those of (Ba,Ca,Sr)$\mathrm{Fe}_2\mathrm{As}_2$ and $\mathrm{Fe}_{1.05}\mathrm{Te}$ (ref. 3), it is important to determine whether spin waves in this material have an overall energy scale similar to other iron-based materials.

Here we use inelastic neutron scattering to map out spin waves in the AF-insulating $\mathrm{Rb}_{0.89}\mathrm{Fe}_{1.58}\mathrm{Se}_2$. We find that although $\mathrm{Rb}_{0.89}\mathrm{Fe}_{1.58}\mathrm{Se}_2$ has a Néel temperature ($T_N=475$ K) much higher than that of the iron pnictides ($T_N\leq 220$ K)[3], spin waves for both classes of materials have similar zone boundary energies[24–26]. However, although itinerant electrons must be considered to understand spin wave properties in the AF iron pnictides[24–26], a local moment Heisenberg Hamiltonian can effectively describe the entire spin wave spectra of the AF $\mathrm{Rb}_{0.89}\mathrm{Fe}_{1.58}\mathrm{Se}_2$. A comparison of the Heisenberg-Hamiltonian-fitted effective exchange couplings in $\mathrm{Rb}_{0.89}\mathrm{Fe}_{1.58}\mathrm{Se}_2$, (Ba,Ca,Sr)$\mathrm{Fe}_2\mathrm{As}_2$ (refs 24–26), and iron chalcogenide $\mathrm{Fe}_{1.05}\mathrm{Te}$ (ref. 27) reveals that their NNN exchange couplings are similar. Therefore, the NNN magnetic interactions in the AF alkaline iron selenides, iron arsenides and iron tellurides, which are robust against the change of electronic band structures, must mainly stem from the superexchange interactions mediated by As/Se(Te), and may have a key role in the magnetism of Fe-based superconductors.

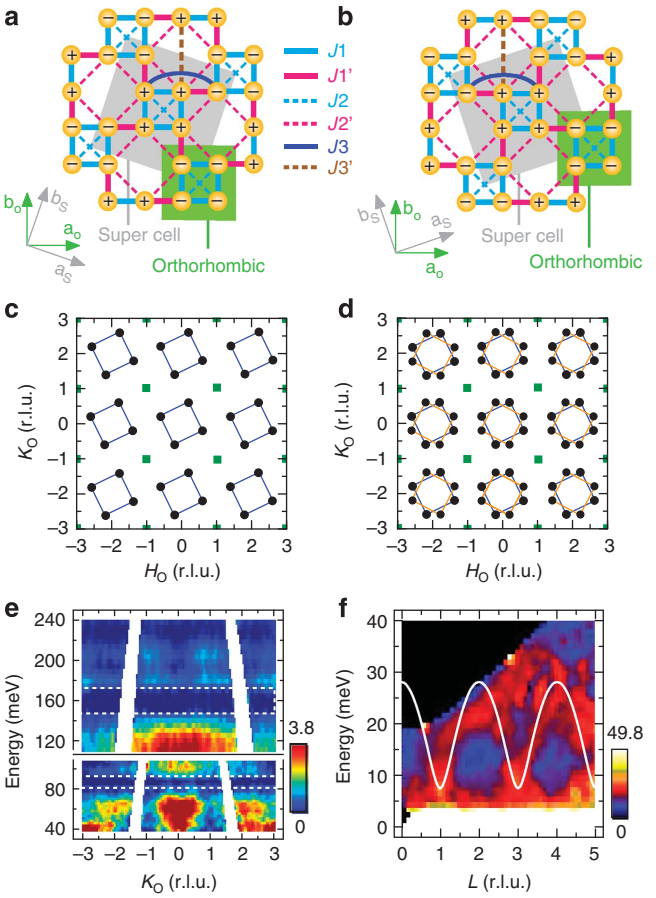

Figure 1 | The antiferromagnetic spin structure and *c*-axis spin waves of the insulating $\mathrm{Rb}_{0.89}\mathrm{Fe}_{1.58}\mathrm{Se}_2$. Our neutron scattering experiments were carried out on the ARCS chopper spectrometer at the Spallation Neutron Source, Oak Ridge National Laboratory. We co-aligned 2.7 g of single crystals grown by self-flux (with mosaic of ~6°). The incident beam energies were $E_i=80,140,250,440$ meV, and mostly with E_i parallel to the *c*-axis. Spin wave intensities were normalized to absolute units using a vanadium standard (with 50% error). We define the wave vector Q at (q_x,q_y,q_z) as $(H_o;K_o;L_o)=(q_xa_o/2\pi;q_ya_o/2\pi;q_zc_o/2\pi)$ r.l.u., where $a_o=5.65$ and $c_o=14.46$ Å are the orthorhombic cell lattice parameters. The AF spin structures are shown for (**a**) left and (**b**) right chirality. The $\sqrt{5}\times\sqrt{5}$ superlattice structure is marked as grey with lattice parameter $a_s=8.933$ Å. The orthorhombic lattice cell is shaded green. The effective nearest neighbour, next nearest neighbour, next-next nearest neighbour exchange couplings are marked as J_1/J'_1, J_2/J'_2, and J_3/J'_3, respectively. (**c**) The $[H_o, K_o]$ reciprocal space with the expected AF Bragg peaks from the left chirality. The green squares show nuclear Bragg peak positions. (**d**) Expected Bragg peaks for both chiralities. (**e**) Spin waves projected onto the K_o-E plane with H_o integration from −2 to −1. The scattering were measured with $E_i=440,250$ meV for top and bottom panels, respectively. (**f**) *c*-axis spin wave dispersion projected on the L–E plane with H_o integration from 0.5 to 0.7 and K integration from 0 to 0.4. The solid line is the calculated *c*-axis dispersion using effective exchange couplings discussed in the main text.

Results

The AF spin structure, reciprocal space, and spin waves. Before carrying out inelastic neutron scattering studies of spin waves in the insulating $\mathrm{Rb}_{0.89}\mathrm{Fe}_{1.58}\mathrm{Se}_2$, we used polarized neutron-diffraction measurements to confirm the previously proposed Fe_4 block AF checkerboard structure (Fig. 1a)[19,22]. As the ferromagnetic (FM) Fe_4 block in the $\sqrt{5}\times\sqrt{5}$ superlattice unit cell can have either left or right chirality (Figs 1a,b), one expects to observe four AF Bragg peaks stemming from each of the chiralities. Fig. 1c shows the expected AF peaks from the left chirality in reciprocal space using the orthorhombic unit cell similar to that of iron pnictides[24–26], where they occur at $(H_o,K_o,L_o)=(0.2+m,0.6+n,L_o);(-0.2+m,-0.6+n;L_o);$ $(0.6+m,-0.2+n,L_o);$ $(-0.6+m,0.2+n,L_o);$ $(m,n=\pm2,\pm4,\ldots,$ and

$L_o = \pm 1, \pm 3, \ldots$). Considering both chiralities for the AF order, there are eight Bragg peaks at wave vectors $(H_o,K_o,L_o) = (\pm 0.2 + m, \pm 0.6 + n, L_o)$ and $(H_o,K_o,L_o) = (\pm 0.6 + m, \pm 0.2 + n, L_o)$ from the block AF checkerboard structure (Fig. 1d), where the odd values of L_o indicate AF coupling along the c-axis direction[19–22]. Therefore, acoustic spin waves in the AF-ordered phase of $Rb_{0.89}Fe_{1.58}Se_2$ should stem from these eight Bragg peaks.

Before mapping out the wave vector dependence of spin waves in $Rb_{0.89}Fe_{1.58}Se_2$, we first determine their overall energy bandwidth and the effective c-axis coupling. Figure 1e shows the background-subtracted scattering projected in the wave vector $(Q = [-1.5, K_o])$ and energy plane. One can see three clear plumes of scattering arising from the in-plane AF zone centres $Q = (0,-2),(0,0)$, and $(0,2)$ r.l.u. With increasing energy, spin waves are gapped at energies between 75 and 95 meV (the bottom panel of Fig. 1e) and between 150 and 170 meV (the top panel of Fig. 1e). The zone boundary spin wave energies are around 220 meV (the top panel of Fig. 1e). Therefore, in spite of the large differences in Néel temperatures and AF structures of $Rb_{0.76}Fe_{1.6}Se_2$ ($T_N = 475$ K)[19–22], $(Ba,Ca,Sr)Fe_2As_2$ ($T_N \leq 220$ K)[24–26], and $Fe_{1.05}Te$ ($T_N \sim 70$ K)[27], their zone boundary spin wave energies are rather similar. To estimate the AF coupling strength along the c-axis, we show in Figure 1f spin waves projected in the wave vector $Q = [0.6,0.2,L_o]$ and energy space. One can see clear dispersive spin waves stemming from AF positions $L_o = 1,3,5$ that reach the zone boundary energy near 30 meV.

Evolution of spin waves. To see the evolution of spin waves with increasing energy, we show in Figure 2 the two-dimensional constant-energy (E) images of spin waves in the $[H_o,K_o]$ plane, for various incident beam energies (E_i). From their c-axis dispersion (Fig. 1f), we know that spin waves in $Rb_{0.89}Fe_{1.58}Se_2$ are three-dimensional, similar to those in $(Ba,Ca,Sr)Fe_2As_2$ (refs 24–26), and centre at AF wave vectors $Q_{AF} = (H_o,K_o,L_o) = (\pm 0.2 + m, \pm 0.6 + n, L)/(\pm 0.6 + m, \pm 0.2 + n, L)$ with $L_o = \pm 1, \pm 3, \ldots$ r.l.u. For an energy transfer of $E = 10 \pm 2$ meV (above the anisotropy gap of $E = 8$ meV, Methods; Supplementary Fig. S1), spin waves are peaked at the expected eight AF Bragg positions Q_{AF} around $Q = (0,0,\pm 1)$ r.l.u. as shown in Figure 2a. On increasing energies to $E = 26 \pm 2$ (Fig. 2b) and 30 ± 2 meV (Fig. 2c), spin waves from the two chiralities centred around the Q_{AF} positions become apparent and increase in size with increasing energy. The two spin wave rings from the left and right AF chiralities (Figs 1a–d) meet near $E = 45 \pm 3$ meV (Fig. 2d). At $E = 55 \pm 3$ meV, the overlapping spin waves from both AF chiralities still form rings around the Q_{AF} positions (Fig. 2e). The spin waves have evolved into broad rings centred around $(H_o,K_o,L_o) = (\pm m, \pm n, L_o)$ at $E = 70 \pm 3$ meV as shown in Figure 2f, just before disappearing into the $75 \leq E \leq 95$ meV spin gap (Fig. 1e). On re-emerging from the spin gap at an energy transfer of 110 ± 10 meV, the spin waves form transversely elongated ellipses centred at the wave vectors $Q = (\pm 1,0)/(0,\pm 1)$ (Fig. 2g), identical to the AF ordering wave vector of $(Ba,Ca,Sr)Fe_2As_2$ (refs 24–26). Finally, at $E = 200 \pm 20$ meV, an energy well above the $150 \leq E \leq 170$ meV spin gap, the spin waves move into wave vectors $Q = (\pm 1,\pm 1)$ (Fig. 2h), almost identical to the zone boundary spin waves for $BaFe_2As_2$ (ref. 24) and $Fe_{1.05}Te$ (ref. 27).

Heisenberg Hamiltonian. We use a local moment Heisenberg Hamiltonian with the effective nearest (NN or J_1,J'_1), next-nearest (NNN or J_2,J'_2), and next-next-nearest neighbour (NNNN or J_3,J'_3) magnetic exchange couplings (Fig. 1a) to fit the observed spin wave spectra[28–32]. To account for the ~8 meV low-energy spin gap (Methods), we add a spin anisotropy term J_s to align spins along the c-axis (Supplementary Eqs S1–S7). There are eight spins in each magnetic unit cell (Fig. 1a,b); therefore, we should have four doubly-degenerate spin wave bands in the Brillouin zone. From Figures 1 and 2, we see that spin waves exist in three separate energy ranges: the lowest branch starts from ~9 meV to ~70 meV,

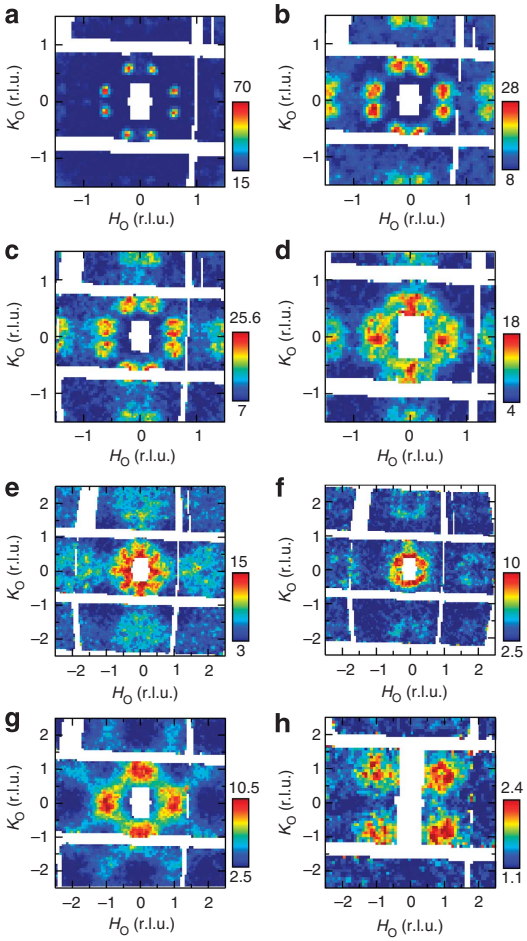

Figure 2 | Wave vector dependence of spin wave excitations at different energies for $Rb_{0.89}Fe_{1.58}Se_2$ at 10 K. Spin wave excitations in the $[H_o, K_o]$ scattering plane at energies (**a**) $E = 10 \pm 2$; (**b**) $E = 26 \pm 2$; (**c**) $E = 30 \pm 2$; (**d**) $E = 45 \pm 3$; (**e**) $E = 55 \pm 3$; (**f**) $E = 70 \pm 3$; (**g**) $E = 110 \pm 10$; and (**h**) $E = 200 \pm 20$ meV. (**a**–**c**), (**d**–**f**),(**g**,**h**) were obtained with $E_i = 80$, 140, 250, and 440 meV, respectively, along the c-axis. The vertical colour bars indicate intensity scale in mbarns per sr per meV per f.u.

the second one from ~80 meV to ~140 meV, and the third branch from ~180 meV to ~230 meV. The high quality spin wave data allows us to place quantitative constraints on effective exchange couplings in the Heisenberg Hamiltonian (Supplementary Eqs. S15–S23). While the low-energy spin waves between ~9 meV and ~70 meV are acoustic modes arising mostly from AF interactions of the FM-blocked spins, the two other branches of excitations are optical spin waves associated with exchange interactions of iron spins within the FM blocks[29–32]. We have attempted, but failed, to fit the entire spin wave spectra using only the effective NN and NNN exchange-coupling Heisenberg Hamiltonian (Fig. 3; Supplementary Figs S1–S4). For spin wave fits that include the NNNN exchange coupling J_3, we find that the low energy spin wave band (acoustic band) depends mainly on J'_1,J'_2,J_3, and J_c (the effective c-axis exchange coupling), but not J_1 and J_2. The second band depends on the J_2 heavily and the top band is mainly determined by J_1.

For simplicity, we consider each FM block with four aligned spins as a net spin S_{eff}. They interact with each other antiferromagnetically (via J_{eff}) to form a cuprates like AF spin structure. There is one spin wave band for this effective block-spin Heisenberg model, which has an analytical form for spin wave dispersion (Supplementary Eq. S15). By comparing the J_{eff} Heisenberg Hamiltonian

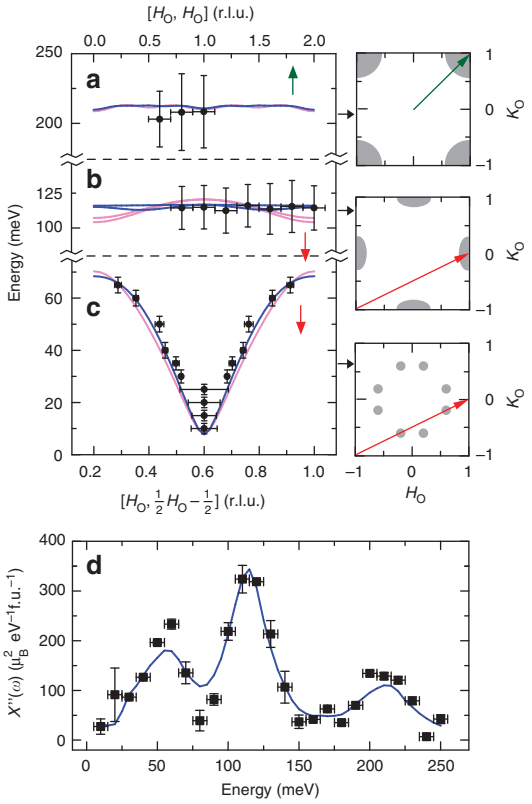

Figure 3 | Spin wave dispersions of $Rb_{0.89}Fe_{1.58}Se_2$ and fits using the Heisenberg Hamiltonian. Spin wave dispersions obtained by cutting along high symmetry directions marked in the right panels for (**a**) highest energy optical-energy band; (**b**) medium-energy optical energy band; and (**c**) acoustic spin wave mode. The blue solid lines show fits with $J_3 > 0$, while the pink solid lines are fits with $J_3 = 0$. (**d**) The energy dependence of the local susceptibility and our model calculation of the local susceptibility. The vertical error bars indicate the statistical errors of one standard deviation.

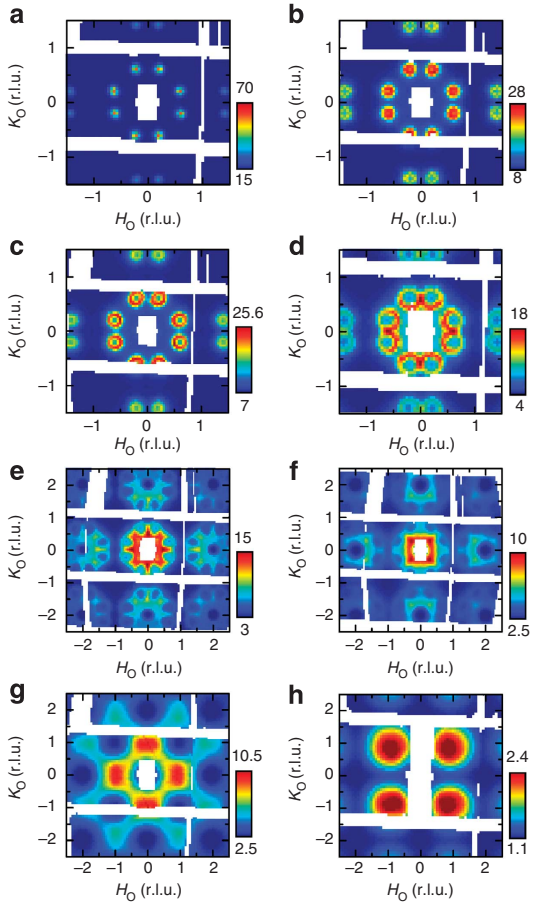

Figure 4 | Calculated energy dependence of the spin waves. The wave vector dependence of the spin waves in the [H_o, K_o] scattering in absolute units for energies of (**a**) $E = 10 \pm 2$; (**b**) $E = 26 \pm 2$; (**c**) $E = 30 \pm 2$; (**d**) $E = 45 \pm 3$; (**e**) $E = 55 \pm 3$; (**f**) $E = 70 \pm 3$; (**g**) $E = 110 \pm 10$; and (**h**) $E = 200 \pm 20$ meV. The instrumental resolution is convoluted with the Heisenberg Hamiltonian.

with those of the J_1-J'_1-J_2-J'_2-J_3-J'_3 model, we find that spin waves in the first band can be approximately described by the J_{eff} Heisenberg Hamiltonian, where $J_{\text{eff}}S_{\text{eff}} = (J'_1 + 2J'_2 + 2J_3)S/4$ is ~17 meV. This suggests that the low energy band is mainly determined by J'_1,J'_2,J_3, and J_c. Physically, the lowest energy band corresponds to the block spin waves where the four spins fluctuate in phase and resemble a single spin. Only at high energies, the relative motions within the blocks can be excited, which correspond to the two high-energy optical modes. Thus, the high-energy bands are basically determined by the intra-block couplings J_1 and J_2.

To quantitatively determine the spin wave dispersion, we determined the measured dispersion from a series of high-symmetry scans through the (H_o,H_o,L_o) and (H_o,1/2H_o – 1/2,L) directions, where L_o was integrated to improve counting statistics. Fig. 3a–c summarize the dispersion of spin waves along the marked directions on the right panels. For the low-energy acoustic mode, we find a spin anisotropy gap below 8 meV and counter propagating spin waves for energies above 30 meV (Fig. 3c). The two high-energy optical spin wave modes are essentially dispersionless. The blue and pink solid lines show Heisenberg Hamiltonian fits to the dispersion curves with and without J_3. The final fitted effective magnetic exchange couplings for spin wave dispersions are $SJ_1 = -36 \pm 2$, $SJ'_1 = 15 \pm 8$, $SJ_2 = 12 \pm 2$, $SJ'_2 = 16 \pm 5$, $SJ_3 = 9 \pm 5$, $J'_3 = 0$, $SJ_c = 1.4 \pm 0.2$, and $SJ_s = 0.44 \pm 0.1$ meV (Supplementary Figs S1–S5 for fits with other parameters). Figure 3d shows the energy dependence of the observed local susceptibility[33] and our calculation using the fitted parameters. We see that the calculated local susceptibility agrees quite well with the data. To further compare the data in Figure 2 with calculated spin waves using fitted effective exchange couplings, we show in Figure 4 the two-dimensional spin wave projections in the [H_o,K_o] plane convoluted with instrumental resolution. The calculated spin wave spectra capture all essential features in the data.

Discussion

For a Heisenberg model with spin S, the total moment sum rule stipulates $M_0 = (g\mu_B)^2 S(S+1)$ (ref. 34). For irons in the $3d^6$ electronic state, the maximum possible moment is $gS = 4\ \mu_B$/Fe for $g = 2$, giving $M_0 = 24\ \mu_B^2$/Fe. On the basis of absolute spin wave intensity measurements in Figure 3d, the sum of the fluctuating moments within the Brillouin zone (Supplementary Fig. S5) below ~250 meV is $\langle m^2 \rangle \sim 16 \pm 3\ \mu_B^2$/Fe. If we assume that the ordered moment is on the order of ~3 μ_B/Fe (refs 19–21), we see that the total moment sum rule is exhausted for magnetic scattering at energies below 250 meV. Therefore, spin waves in insulating $Rb_{0.76}Fe_{1.63}Se_2$ can be regarded as a classic local moment system where a Heisenberg Hamiltonian is an appropriate description of spin wave spectra. For comparison, we note that the sum of the fluctuating local moments throughout the Brillouin zone for AF metallic $BaFe_2As_2$ (ref. 24) and superconducting $BaFe_{1.9}Ni_{0.1}As_2$ (ref. 35) are $\langle m^2 \rangle = 3.17 \pm 0.16$ and $3.2 \pm 0.16\ \mu_B^2$ per Fe(Ni), respectively (M.S. Liu *et al.*, unpublished results). Because $\langle m^2 \rangle$ for iron pnictides are much less than that of the insulating

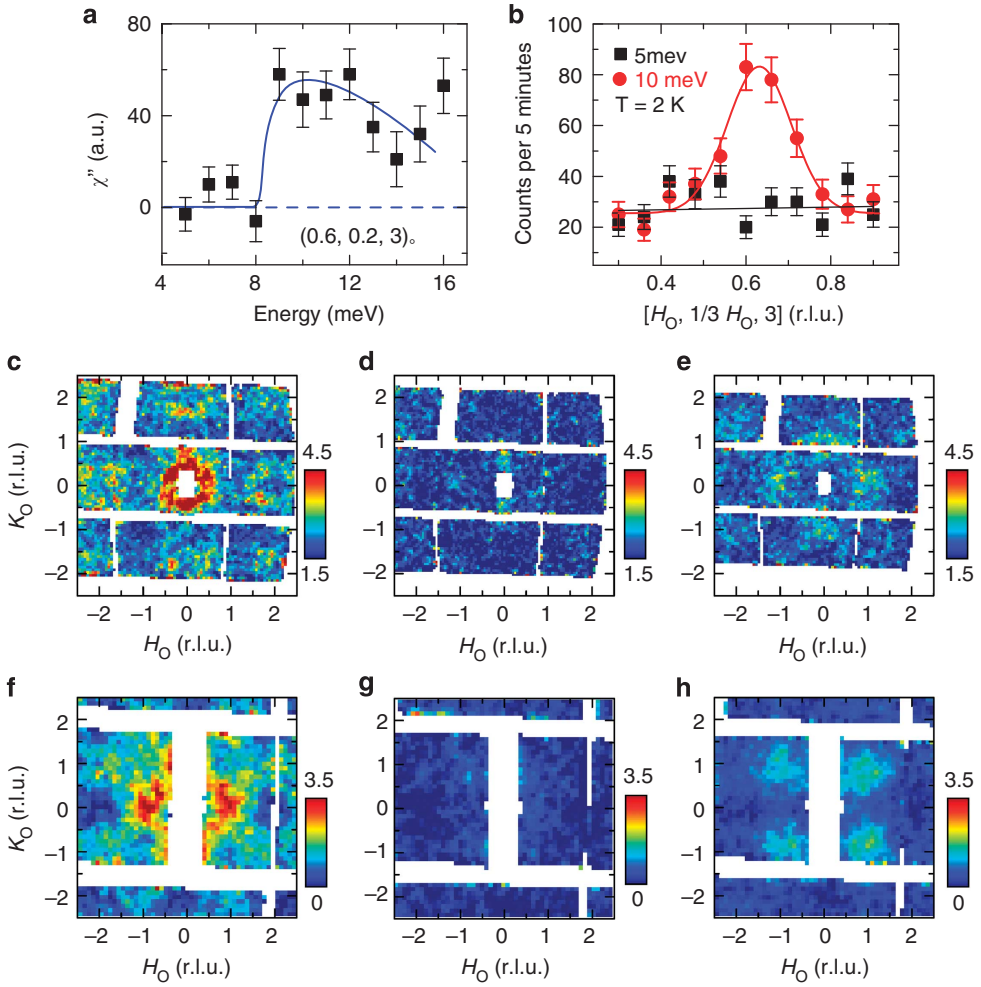

Figure 5 | Triple-axis spectrometer data and extra spin wave images near spin gaps on $Rb_{0.89}Fe_{1.58}Se_2$. (**a**) Constant-Q scan at the AF wave vector Q_{AF} = (0.6,0.2,3) r.l.u. with background subtracted, and corrected for Bose population factor. There is a clear spin gap below E = 8 meV. The data were collected on HB-1 triple-axis spectrometer. (**b**) Constant-energy scans across the AF wave vector at E = 5 meV and E = 10 meV. The data confirm the presence of a spin gap at 5 meV. The vertical error bars indicate the statistical errors of one standard deviation. Spin wave images in the (H_o,K_o) plane for energy transfers of (**c**) E = 74±4; (**d**) 82±4;(**e**) 90±4; (**f**) 140±10; (**g**) 155±15; (**h**) 195±15 meV. There are clearly no spin wave excitations at E = 82±4 and 155±15 meV.

alkaline iron selenides, there must be significant hybridization of Fe 3*d* with pnictide *p* orbitals and, among themselves, in iron pnictides, which leads to a metallic state where the Hund's coupling is less important than in the atomic limit[36]. This is consistent with the fact that a pure Heisenberg Hamiltonian cannot describe the entire spin wave spectra in AF iron pnictides[24–26] and iron chalcogenide $Fe_{1.05}Te$ (ref. 27).

It is instructive to compare the effective magnetic exchange couplings in different AF parent compounds of iron-based superconductors. First, comparing $Rb_{0.89}Fe_{1.58}Se_2$ with $Fe_{1.05}Te$ (ref. 27), we note that, although their static AF orders have completely different structures, these two iron chalcogenides are very similar in terms of the values of their effective exchange couplings. Both of them have, first, large FM J_1 (or J_{1a}); second, large anisotropy between the two NN couplings J_1(J_{1a}) and J_1' (or J_{1b}); and, third, AF NNN couplings and small anisotropy between two NNN couplings J_2 (or, J_{2a}) and J_2' (or J_{2b}). Finally, there are significant AF–NNNN couplings J_3. Therefore, the presence of the iron vacancy ordering in $Rb_{0.89}Fe_{1.58}Se_2$ reduces magnetic frustration and stabilizes the block AF structure, but does not change the local magnetic exchange coupling strengths as compared with $Fe_{1.05}Te$, even though the 5*p* orbitals of Te should be larger than the 4*p* orbitals of Se. Second, comparing $Rb_{0.89}Fe_{1.58}Se_2$ to iron-pnictides, we find that there are important differences as well as essential common features: the differences include the large differences in the sum of the fluctuating local moments $\langle m^2 \rangle$ and the NN exchange couplings. However, the NNN exchange couplings are rather similar in spite of their insulating and metallic ground states.

To summarize, whereas the NN exchange couplings vary significantly according to the spin configurations between the corresponding two NN sites in the magnetically ordered states of alkaline iron selenides, iron tellurides, and iron pnictides, the AF–NNN exchange coupling remains almost uniform for these materials. This is consistent with the idea that the NNN coupling J_2 is mainly determined by a local superexchange mechanism mediated by As or Se/Te (ref. 37). Therefore, regardless of their metallic or insulating ground states, different AF structures and Néel temperatures, spin waves in all parent compounds of Fe-based superconductors have a similar energy scale with a common NNN magnetic coupling controlled by the local superexchange interactions. As superconductivity in Fe-based materials arises from electron or hole-doping of their AF parent compounds, the similarities in the magnetic properties of parent

compounds suggest that the microscopic origin of superconductivity for doped superconductors should be similar as well.

Methods

Single-crystal $Rb_{0.89}Fe_{1.58}Se_2$. Our single crystals of $Rb_yFe_{1.6+x}Se_2$ were grown using flux method. High-purity Fe, Se and Rb were mixed in appropriate stoichiometry and placed inside an alumina crucible. The crucible was sealed in Ar-filled silica ampoule. The mixture was heated to 950 °C for 5 h followed by 5 °C per hr cooling down to 900 °C, and then furnace cooling down to room temperature[11]. The actual crystal composition of $Rb_{0.89}Fe_{1.58}Se_2$ was determined inductively coupled plasma analysis.

Extra spin wave data. In addition to the time-of-flight measurements presented in Figures 1–4, we have taken triple-axis spectrometer measurements on HB-1 at High Flux isotope reactor, Oak Ridge National Laboratory, to determine the low-energy spin-anisotropy gap. Before showing the results, we note that, although the scattering cross-section is related to the dynamic structure factor $S(Q,E)$, it is proportional to the imaginary part of the dynamic susceptibility $\chi''(Q,\omega)$ if the temperature is much lower than the lowest energy spin waves. Theoretically, one has $S(Q,E) = 1/(1-\exp(-E/(k_BT)))\chi''(Q,E)$. If $k_BT \ll E$, as is the case of the experiment, one has $S(Q,E) \propto \chi''(Q,E)$. Figure 5a shows $\chi''(Q,E)$ at $Q_{AF} = (0.6,0.2,3)$, which clearly establishes the anisotropy spin gap of ~8 meV. Constant energy scans at 5 meV and 10 meV, shown in Figure 5b, confirm the presence of the spin gap below 8 meV. To further demonstrate the presence of spin gaps around 80 and 160 meV, we show, in Figure 5c–e, constant energy cuts for energies of $E = 74 \pm 4$ meV, 82 ± 4 meV, and 90 ± 4 meV, respectively. There are clearly no magnetic scattering near $E = 82 \pm 4$ meV (Fig. 5d). Figure 5f–h show similar constant-energy images at $E = 140 \pm 10$, 155 ± 15, and 195 ± 15 meV. The scattering near $E = 155 \pm 15$ meV are featureless, confirming the presence of a spin gap at this energy.

References

1. Kamihara, Y., Watanabe, T., Hirano, M. & Hosono, H. Iron-based layered superconductor $La[O_{1-x}F_x]FeAs$ (x=0.05 – 0.12) with T_c=26 K. *J. Am. Chem. Soc.* **130,** 3296–3297 (2008).
2. Mazin, I. I. Superconductivity gets an iron boost. *Nature* **464,** 183–186 (2010).
3. Johnston, D. C. The puzzle of high temperature superconductivity in layered iron pnictides and chalcogenides. *Adv. Phys.* **59,** 803–1061 (2010).
4. de la Cruz, C. *et al.* Magnetic order close to superconductivity in the iron-based layered $LaO_{1-x}F_xFeAs$ systems. *Nature* **453,** 899–902 (2008).
5. Maier, T. A. & Scalapino, D. J. Theory of neutron scattering as a probe of the superconducting gap in the iron pnictides. *Phys. Rev. B* **78,** 020514(R) (2008).
6. Korshunov, M. M. & Eremin, I. Theory of magnetic excitations in iron-based layered superconductors. *Phys. Rev. B* **78,** 140509(R) (2008).
7. Christianson, A. D. *et al.* Resonant Spin Excitation in the High Temperature Superconductor $Ba_{0.6}K_{0.4}Fe_2As_2$. *Nature* **456,** 930–932 (2008).
8. Guo, J. G. *et al.* Superconductivity in the iron selenide $K_xFe_2Se_2$ ($0 \le x \le 1.0$). *Phys. Rev. B* **82,** 180520(R) (2010).
9. Krzton-Maziopa, A. *et al.* Synthesis and crystal growth of $Cs_{0.8}(FeSe_{0.98})_2$: a new iron-based superconductor with T_c=27 K. *J. Phys. Condens. Matter* **23,** 052203 (2011).
10. Fang, M. H. *et al.* Fe-based high temperature superconductivity with T_c=31 K bordering an insulating antiferromagnet in $(Tl,K)Fe_xSe_2$ Crystals. *Europhys. Lett.* **94,** 27009 (2011).
11. Wang, A. F. *et al.* Superconductivity at 32 K in single crystal $Rb_{0.78}Fe_2Se_{1.78}$. *Phys. Rev. B* **83,** 060512 (2011).
12. Wang, D. M., He, J. B., Xia, T.- L. & Chen, G. F. Effect of varying iron content on the transport properties of the potassium-intercalated iron selenide $K_xFe_{2-y}Se_2$. *Phys. Rev. B* **83,** 132502 (2011).
13. Zhang, Y. *et al.* Heavily electron-doped electronic structure and isotropic superconducting gap in $A_xFe_2Se_2$ (A=K,Cs). *Nature Mater.* **10,** 273–277 (2011).
14. Qian, T. *et al.* Absence of holelike Fermi surface in superconducting $K_{0.8}Fe1.7Se_2$ revealed by ARPES. *Phys. Rev. Lett.* **106,** 187001 (2011).
15. Mou, D. X. *et al.* Distinct fermi surface topology and nodeless superconducting gap in $(Tl_{0.58}Rb_{0.42})Fe_{1.72}Se_2$ superconductor. *Phys. Rev. Lett.* **106,** 107001 (2011).
16. Mazin, I. I. Iron superconductivity weathers another storm. *Physics* **4,** 26 (2011).
17. Häggström, L., Seidel, A. & Berger, R. A Mössbauer study of antiferromagnetic ordering in iron deficient $TlFe_{2-x}Se_2$. *J. Magn. Magn. Mater.* **98,** 37–46 (1991).
18. Bacsa, J. *et al.* Cation vacancy order in the $K_{0.8+x}Fe_{1.6-y}Se_2$ system: five-fold cell expansion accommodates 20% tetrahedral vacancies. *Chem. Sci.* **2,** 1054 (2011).
19. Bao, W. *et al.* A novel large moment antiferromagnetic order in $K_{0.8}Fe_{1.6}Se_2$ Superconductor. *Chinese Phys. Lett.* **28,** 086104 (2011).
20. Yu, V. *et al.* Iron vacancy superstructure and possible room temperature antiferromagnetic order in superconducting $Cs_yFe_{2-x}Se_2$. *Phys. Rev. B* **83,** 144410 (2011).
21. Bao, W. *et al.* Vacancy tuned magnetic high-T_c superconductor $K_xFe_{2-x/2}Se_2$. Preprint arXiv:1102.3674 (2011).
22. Wang, M. *et al.* Antiferromagnetic order and superlattice structure in nonsuperconducting and superconducting $Rb_yFe_{1.6+x}Se_2$. *Phys. Rev. B* **84,** 094504 (2011).
23. Seo, K., Bernevig, B. A. & Hu, J. P. Pairing symmetry in a two-orbital exchange coupling model of oxypnictides. *Phys. Rev. Lett.* **101,** 206404 (2008).
24. Harriger, L. W. *et al.* Nematic spin fluid in the tetragonal phase of $BaFe_2As_2$. *Phys. Rev. B* **84,** 054544 (2011).
25. Zhao, J. *et al.* Spin waves and magnetic exchange interactions in $CaFe_2As_2$. *Nat. Phys.* **5,** 555–560 (2009).
26. Ewings, R. A. *et al.* Itinerant spin excitations in $SrFe_2As_2$ measured by inelastic neutron scattering. *Phys. Rev. B* **83,** 214519 (2011).
27. Lipscombe, O. J. *et al.* Spin waves in the (π,0) magnetically ordered iron chalcogenide $Fe_{1.05}Te$. *Phys. Rev. Lett.* **106,** 057004 (2011).
28. Cao, C. & Dai, J. Block spin ground state and 3-dimensionality of $(K,Tl)Fe_{1.6}Se_2$. *Phys. Rev. Lett.* **107,** 056401 (2011).
29. You, Y. Z., Yao, H. & Lee, D.- H. The spin exictations of the block-antiferromagnetic $K_{0.8}Fe_{1.6}Se_2$. *Phys. Rev. B* **84,** 020406 (2011).
30. Fang, C., Xu, B., Dai, P. C., Xiang, T. & Hu, J. P. Magnetic frustration and iron-vacancy ordering in iron chalcogenide. Preprint arXiv:1103.4599 (2011).
31. Lu, F. & Dai, X. Spin waves in the block checkerboard antiferromagnetic phase. Preprint arXiv:1103.5521 (2011).
32. Yu, R., Goswami, P. & Si, Q. The magnetic phase diagram of an extended J_1-J_2 model on a modulated square lattice and its implications for the antiferromagnetic phase of $K_yFe_xSe_2$. *Phys. Rev. B* **84,** 094451 (2011).
33. Lester, C. *et al.* Dispersive spin fluctuations in the nearly optimally doped superconductor $Ba(Fe_{1-x}Co_x)_2As_2$ (x=0.065). *Phys. Rev. B* **81,** 064505 (2010).
34. Lorenzana, L., Seibold, G. & Coldea, R. Sum rules and missing spectral weight in magnetic neutron scattering in the cuprates. *Phys. Rev. B* **72,** 224511 (2005).
35. Wang, M. Y. *et al.* Electron-doping evolution of the low-energy spin excitations in the iron arsenide superconductor $BaFe_{2-x}Ni_xAs_2$. *Phys. Rev. B* **81,** 174524 (2010).
36. Cvetkovic, V. & Tesanovic, Z. Multiband magnetism and superconductivity in Fe-based compounds. *Europhys. Lett.* **85,** 37002 (2009).
37. Si, Q. & Abrahams, E. Strong correlations and magnetic frustration in the high T_c iron pnictides. *Phys. Rev. Lett.* **101,** 076401 (2008).

Acknowledgements

We thank Masaaki Matsuda for his help on triple-axis measurements. The neutron-scattering work at UTK is supported by the US NSF-DMR-1063866 and NSF-OISE-0968226. The single-crystal growth effort at UTK is supported by US DOE BES under Grant No. DE-FG02-05ER46202. ORNL neutron scattering facilities are supported by the US DOE, Division of Scientific User Facilities. Work at IOP is supported by the Chinese Academy of Sciences and by the Ministry of Science and Technology of China 973 program (2012CB821400). D.X.Y. is supported by NSFC-11074310.

Author contributions

P.D. and M.Y.W. planned neutron-scattering experiments. M.Y.W., L.W.H., T.N., C.L.Z., M.W., M.B.S. and P.D. carried out neutron-scattering experiments. Data analysis was done by C.F., D.X.Y., M.Y.W., L.W.H., with help from J.P.H. The samples were grown by G.T.T., Y.S.and T.N., C.L.Z., and co-aligned by M.Y.W. and W.T. The paper was written by P.D., W.Y.W., C.F. and J.P.H. with input from M.B.S. and D.X.Y. All co-authors provided comments on the paper.

Additional information

Supplementary Information accompanies this paper at http://www.nature.com/naturecommunications

Competing financial interests: The authors declare no competing financial interests.

Reprints and permission information is available online at http://npg.nature.com/reprintsandpermissions/

How to cite this article: Wang, M. *et al.* Spin waves and magnetic exchange interactions in insulating $Rb_{0.89}Fe_{1.58}Se_2$. *Nat. Commun.* 2:580 doi: 10.1038/ncomms1573 (2011).

Supplementary Figures:

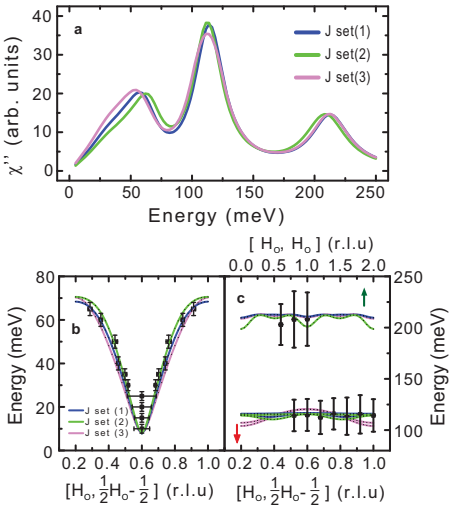

Supplementary Fig. S1: Calculated local susceptibility and dispersion curves for three different exchange parameters. (a) Energy dependence of the imaginary part of local susceptibility for the three different exchange parameter sets. (b,c) Dispersion curves for the three different exchange parameter sets as discussed in the text.

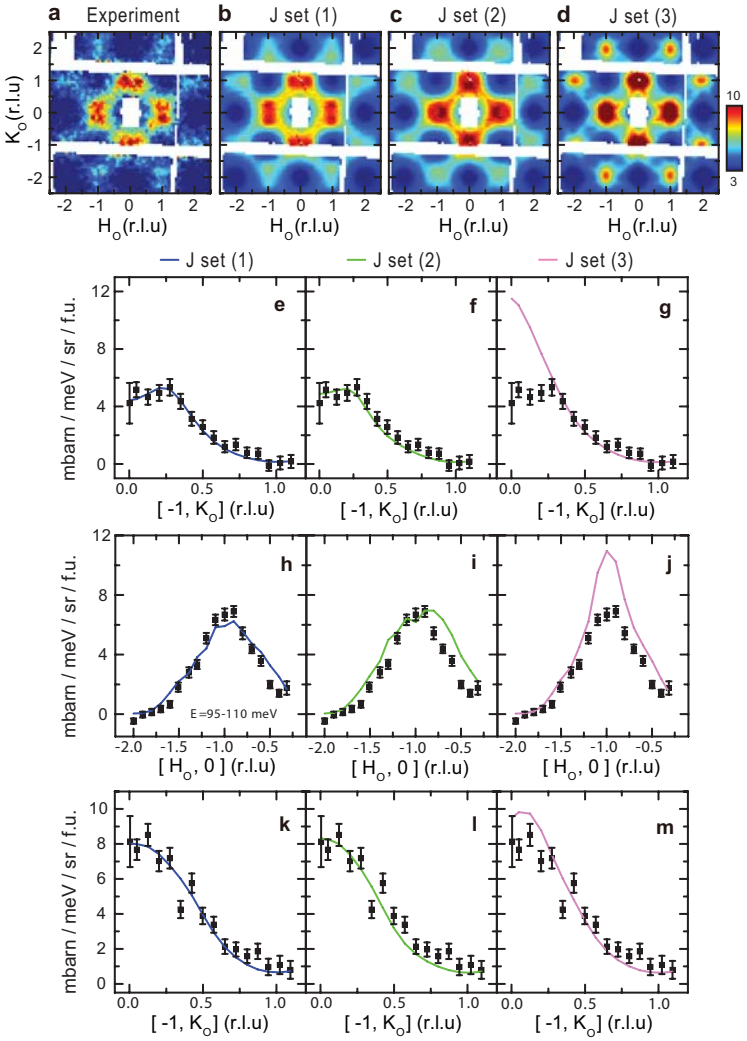

Supplementary Fig. S2: Calculated dynamic structure factor and their comparison with Heisenberg Hamiltonian with different exchange parameters. (a) Constant energy cut of data at $E = 102.5 \pm 7.5$ meV projected onto the (H_o, K_o) plane. (b,c,d) Calculated dynamic structure factor $S(q, \omega = 102.5 \pm 7.5)$ projected onto the (H_o, K_o) plane for three different exchange coupling parameters. (e-m) Cuts along different directions and their comparison with spin wave calculations in three different exchange coupling parameters.

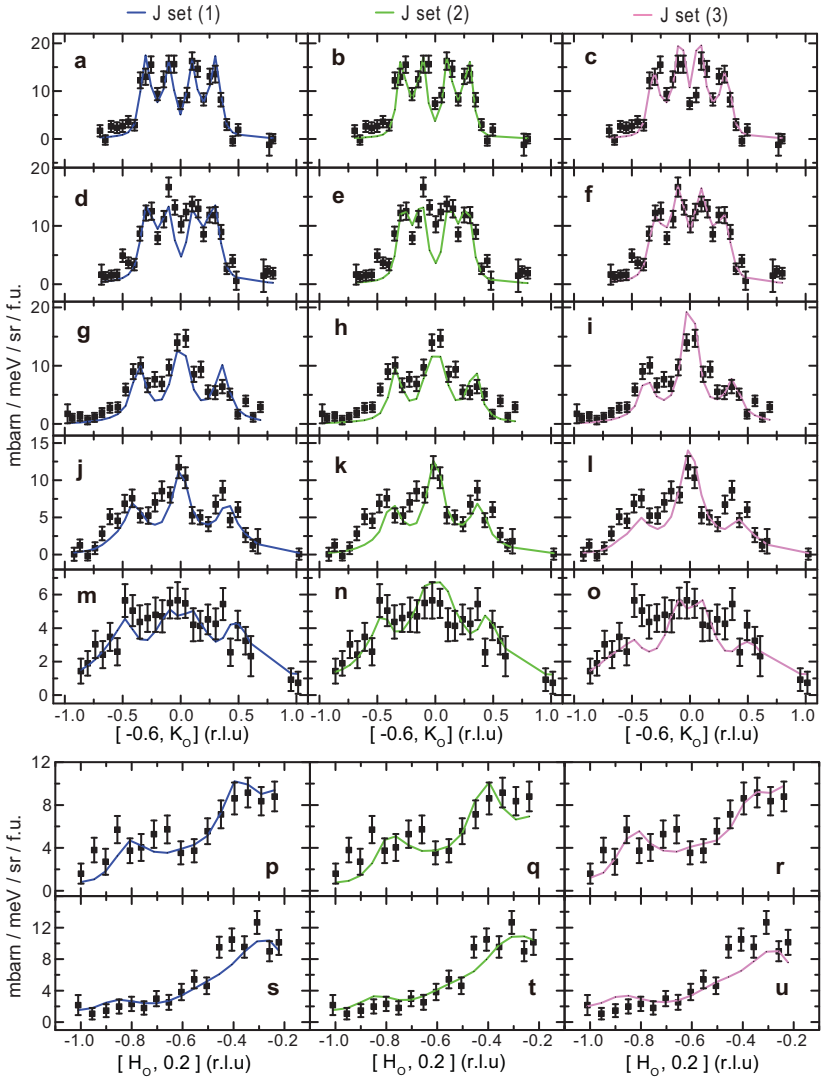

Supplementary Fig. S3: Spin-wave dispersions of $Rb_{0.89}Fe_{1.58}Se_2$ and fits using the Heisenberg Hamiltonian with three different exchange coupling parameters as discussed in the text. Spin-wave dispersions in the acoustic branch obtained by cutting along high-symmetry directions and model fits using three different sets of exchange coupling parameters (a)-(o) Cuts along the $[-0.6, K_o]$ direction by integrating H_o from -0.65 to -0.55. (p)-(u) Cut along $[H_o, 0.2]$ direction by integrating K_o from 0.15 to 0.25.

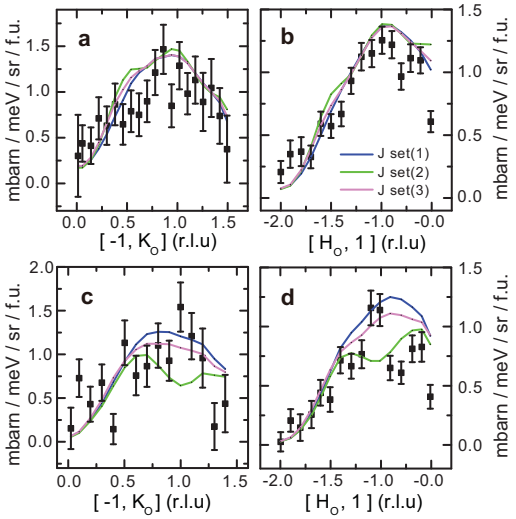

Supplementary Fig. S4: Spin-wave cuts of $Rb_{0.89}Fe_{1.58}Se_2$ and fits using the Heisenberg Hamiltonian with three sets of parameters. Q-cuts for the highest branch. The H_o integration range in (a),(c) is from -1.05 to -0.95. Integration of the K_o range in (b),d) is from 0.8 to 1.2.

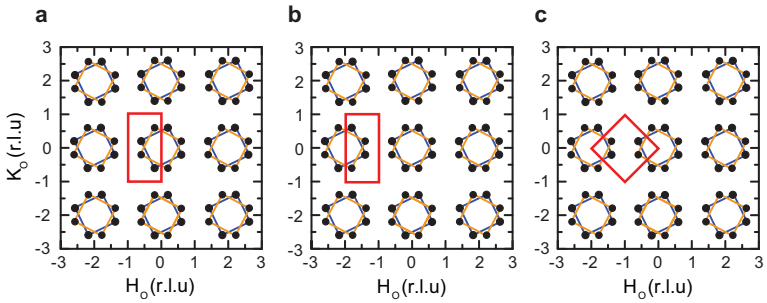

Supplementary Fig. S5: Red squares show wave vector integration area used for determining the local dynamic susceptibility $\chi''(\omega)$ at different energies. For $E_i = 80$ meV, we use (a) for $E = 10$-20 meV; (b) 30-50 meV; $E_i = 140$ meV, $E = 30$-90 meV; $E_i = 250$ meV, $E = 40$-90 meV; (c) $E_i = 250$ meV, $E = 90$-150 meV; $E_i = 440$ meV, $E = 100$-250 meV. We chose area (b) for $E = 30$-90 meV becuase spin wave intensity at this energy region is mainly distributed near $Q = (0, 0)$, which is partially blocked by the main beam. For $E = 90$-150 meV, we chose area (c) because at these energies, some of the detectors in area (a) do not give correct intensity, and comparing with area (b), data in area (c) have better statisitcs and lower background.

Supplementary Notes:

Supplementary Note 1. Model Heisenberg Hamiltonian

The model we use to understand the magnetic excitation is a quantum spin model with up to third nearest neighbor (NNNN) exchange in the ab-plane, nearest neighbor (NN) exchange along the c-axis and a single ion anisotropy term, i.e.,

$$H = H_{ab} + H_c + H_s, \tag{S1}$$

where

$$\begin{aligned} H_c &= J_c \sum_r \mathbf{S}_r \cdot \mathbf{S}_{r+z}, \\ H_s &= \frac{J_s}{2} \sum_r (S^2_{r,x} + S^2_{r,y}), \end{aligned} \tag{S2}$$

and H_{ab} is given in Ref. [30]. To solve the Hamiltonian, one can use the standard linear spin wave approach. A generic position of the spin is given by

$$\mathbf{r} = m\mathbf{l_1} + n\mathbf{l_2} + \mathbf{d_i}, \tag{S3}$$

where m, n are integers and

$$\begin{aligned} \mathbf{l_1} &= (2\mathbf{x} - \mathbf{y})/\sqrt{5}, \\ \mathbf{l_2} &= (\mathbf{x} + 2\mathbf{y})/\sqrt{5}, \\ \mathbf{d_1} = 0,\ \mathbf{d_2} &= \mathbf{x},\ \mathbf{d_3} = \mathbf{x} + \mathbf{y},\ \mathbf{d_4} = \mathbf{y}. \end{aligned} \tag{S4}$$

The Holstein-Primakoff transform (truncated) of the spin operators is given by
For $m + n$ =even:

$$\begin{aligned} S_+(\mathbf{r}) &= \sqrt{2S} a_i(\mathbf{R}), \\ S_-(\mathbf{r}) &= \sqrt{2S} a_i^\dagger(\mathbf{R}), \\ S_z(\mathbf{r}) &= S - a_i^\dagger(\mathbf{R}) a_i(\mathbf{R}); \end{aligned} \tag{S5}$$

For $m + n$ =odd:

$$\begin{aligned} S_+(\mathbf{r}) &= \sqrt{2S} a_i^\dagger(\mathbf{R}), \\ S_-(\mathbf{r}) &= \sqrt{2S} a_i(\mathbf{R}), \\ S_z(\mathbf{r}) &= -S + a_i^\dagger(\mathbf{R}) a_i(\mathbf{R}). \end{aligned} \tag{S6}$$

Define $\psi^\dagger(k) = (a_1^\dagger(k), a_2^\dagger(k), a_3^\dagger(k), a_4^\dagger(k), a_1(-k), a_2(-k), a_3(-k), a_4(-k))$, and we have

$$H = \frac{1}{2} \sum_k \psi^\dagger(k) \begin{pmatrix} A(k) & B(k) \\ B(k) & A(k) \end{pmatrix} \psi(k). \tag{S7}$$

$A(k)$ and $B(k)$ are four-by-four matrices, defined by:

$$A(k) = S \begin{pmatrix} E_0 & J_1 e^{ik_x} & J_2 e^{ik_x + ik_y} + J_3' e^{-i2k_x} & J_1 e^{ik_y} \\ \cdot & E_0 & J_1 e^{ik_y} & J_2^{-ik_x + ik_y} + J_3' e^{-2ik_y} \\ \cdot & \cdot & E_0 & J_1 e^{-ik_x} \\ \cdot & \cdot & \cdot & E_0 \end{pmatrix}, \tag{S8}$$

$$B(k) = S \begin{pmatrix} 2J_c \cos(k_z) & J_2' e^{-ik_x + ik_y} + J_3 e^{-2ik_y} & J_1' e^{-ik_y} & J_2' e^{-ik_x - ik_y} + J_3 e^{2ik_x} \\ \cdot & 2J_c \cos(k_z) & J_2' e^{-ik_x - ik_y} + J_3 e^{2ik_x} & J_1' e^{ik_x} \\ \cdot & \cdot & 2J_c \cos(k_z) & J_2' e^{ik_x - ik_y} + J_3 e^{2ik_y} \\ \cdot & \cdot & \cdot & 2J_c \cos(k_z) \end{pmatrix}, \tag{S9}$$

where $E_0 = -(2J_1 + J_2 - J_1' - 2J_2' - 2J_3 + J_3' - 2J_c - J_s)S$. The lower triangle elements are suppressed because both matrices are hermitian.

We use equations of motion to solve this Hamiltonian.

$$\partial\psi(k)/\partial t = -i \begin{pmatrix} A(k) & B(k) \\ -B(k) & -A(k) \end{pmatrix} \psi(k). \tag{S10}$$

Solving this eigenvalue problem for each k, we have

$$H = \sum_{i=1,2,3,4;k} (\gamma_i^\dagger(k)\gamma_i(k) + 1/2)\omega_i(k), \tag{S11}$$

and

$$a_i(k) = \sum_j U_{ij}(k)\gamma_j(k) + V_{ij}(k)\gamma_j^\dagger(-k). \tag{S12}$$

The differential cross section of inelastic neutron scattering can be expressed in terms of the spin wave dispersion and wave functions:

$$\sigma(\omega, q) = I_0(\omega, q)(1 + n_B(\omega, T)) \sum_\alpha |\sum_i U_{i\alpha}(q) + V_{i\alpha}^\star(-q)|^2 D(\omega, \omega_\alpha). \tag{S13}$$

In the above expression, $I_0(\omega, q)$ includes all factors of experimental resolution extracted from information of each detector, $n_B(\omega, T)$ is the Bose factor and $D(\omega, \omega_\alpha)$ is the harmonic oscillator damping given by

$$D(\omega, \omega_0) = \frac{4}{\pi} \frac{\omega\omega_0\Gamma(\omega)}{(\omega^2 - \omega_0^2)^2 + 4\Gamma(\omega)^2\omega^2}. \tag{S14}$$

The damping strength $\Gamma(\omega)$ is approximated by a linear function of energy whose explicit form is to be fitted. Our fitting is based on so far the most general spin model with all symmetry allowed exchanges up to NNNN. A failure of this model in understanding the data would mean that the observed excitations cannot be explained by a local moment picture and the effect of itinerant electrons must be seriously considered.

Supplementary Note 2. Fitting constraints

The high quality of the data allows one to place quantitative constraints on parameters in the model. The data shows that the excitations exist in three separate energy ranges. The lowest branch starts from $\sim$ 9 meV to $\sim$ 70 meV, second from $\sim$ 100 meV to $\sim$ 140 meV and the third branch from $\sim$180 meV to $\sim$230 meV. The low energy part of the first branch can be fitted very well by the form

$$\epsilon(k) = \sqrt{\Delta_s^{exp2} + v_s^{exp2}k^2}, \tag{S15}$$

with $v_s^{exp} = 300$ meV $\cdot$ Å and $\Delta_s^{exp} = 9$ meV. At the propagation vector of the ground state $Q = (0.6, 0.2, 1)$ rlu (in the orthorhombic basis), energy has k_z dispersion, and the band top is about E_c^{exp} $\sim$30 meV. All these values have analytical expressions in the spin wave model. The anisotropy gap (bottom of the first branch) is

$$\Delta_s = S\sqrt{J_s(2J_1' + 4J_2' + 4J_3 + 4J_c + J_s)}. \tag{S16}$$

The top of the first band is reached at $Q_o = (0.2, 0.4, 0)$ rlu with

$$\begin{aligned} E_{1t} \;=\; & 2S[2J_1^2 + J_1'(J_2' + J_3 - J_3' + J_c) + (J_2' + J_3 - J_3')(J_2' + J_3 - J_3' + 2J_c) - J_1(J_1' + 2(J_2' + J_3 - J_3' + J_c)) \\ & -\sqrt{4J_1^4 + {J_1'}^2 J_c^2 + 4J_1^2(J_2' + J_3 - J_3' + J_c)(J_1' + J_2' + J_3 - J_3' + J_c) - 4J_1^3(J_1' + 2(J_2' + J_3 - J_3' + J_c))}]^{\frac{1}{2}}. \end{aligned} \tag{S17}$$

Without single ion anisotropy, i.e., $J_s = 0$, the spin wave velocity is given by

$$\begin{aligned} v_s = \sqrt{\frac{5}{2}}S\{&[J_1(J_1' + 2(J_2' + J_3 - J_3')) + J_1'(J_2 - J_2' - J_3 + J_3') + 2(J_2(J_2' + J_3 - J_3') + 2J_3(J_3' - J_2'))] \\ & (J_1' + 2(J_2' + J_3 + J_c))/(J_1 - J_1' + J_2 - J_2' - J_3 + J_3')\}^{1/2}. \end{aligned} \tag{S18}$$

The expression with $J_s \neq 0$ is also available but too lengthy to be placed here, and interested readers can request it from the authors. The second branch actually contains two close spin wave bands. The branch starts at $Q = (0.3, 0.1, 1)$ rlu with energy E_{2b}, whose expression is again too lengthy to be published. The second branch ends at $\Gamma = (0, 0, 0)$ point with

$$E_{2t} = S\sqrt{(2J_1 - 2J_1' + 2J_2 - 2J_2' - 2J_3 + 2J_3' - J_s)(2J_1 + 2J_2 - 2J_2' - 2J_3 + 2J_3' - 4J_c - J_s)}. \tag{S19}$$

The highest branch starts at Γ point with

$$E_{3b} = S\sqrt{(4J_1 - 4J_2' - 4J_3 - J_s)(4J_1 - 2J_1' - 4J_c - J_s)}, \tag{S20}$$

and ends at $(0.2, 0.4, 0)$ with

$$\begin{aligned} E_{3t} &= 2S[2J_1^2 + J_1'(J_2' + J_3 - J_3' + J_c) + (J_2' + J_3 - J_3')(J_2' + J_3 - J_3' + 2J_c) - J_1(J_1' + 2(J_2' + J_3 - J_3' + J_c)) \\ &+ \sqrt{4J_1^4 + {J_1'}^2 J_c^2 + 4J_1^2(J_2' + J_3 - J_3' + J_c)(J_1' + J_2' + J_3 - J_3' + J_c) - 4J_1^3(J_1' + 2(J_2' + J_3 - J_3' + J_c))}]^{\frac{1}{2}}. \end{aligned} \tag{S21}$$

The band top along the c-axis is reached at $(0.6, 0.2, 0)$ with

$$E_c = S\sqrt{[2(J_1' + 2J_2' + 2J_3) - J_s](4J_c + J_s)}. \tag{S22}$$

Based on the data and considering the effect of large damping at high energies, we have for the above quantities the following constraints:

$$\begin{aligned} \Delta_s &= \Delta_s^{exp} = 8 \sim 12 \text{ meV}, \\ v_s &= v_s^{exp} = 250 \sim 300 \text{ meV} \cdot \text{Å}, \\ E_{1t} &= 60 \sim 75 \text{ meV}, \\ E_{2b} &= 90 \sim 110 \text{ meV}, \\ E_{2t} &= 110 \sim 130 \text{ meV}, \\ E_{3b} &= 180 \sim 200 \text{ meV}, \\ E_{3t} &= 200 \sim 220 \text{ meV}, \\ E_c &= 25 \sim 30 \text{ meV}. \end{aligned} \tag{S23}$$

Supplementary Note 3. Fitting parameters

The above constraints give a very narrow range of parameters, we can further constraint possible exchange constants so that a quantitative fit to the data shown in the paper can be found. In this section we discuss what elements are indispensable to our fittings.

We first emphasize that a proper fitting should have $J_3 > 0$ and $J_1' > 0$ (antiferromagnetic). To see this, we compare the following possible parameters since they can all approximately describe the data:

(1) $SJ_1 = -36$, $SJ_1' = 15$, $SJ_2 = 12$, $SJ_2' = 16$, $SJ_3 = 9.5$, $SJ_3' = 0$, $SJ_c = 1.4$, $SJ_s = 0.44$ meV. (2) $SJ_1 = -36$, $SJ_1' = -5.7$, $SJ_2 = 13.4$, $SJ_2' = 22.4$, $SJ_3 = 14.2$, $SJ_3' = 0$, $SJ_c = 1.4$, $SJ_s = 0.44$ meV. (3) $SJ_1 = -36$, $SJ_1' = 10$, $SJ_2 = 11$, $SJ_2' = 28.7$, $SJ_3 = 0$, $SJ_3' = 0$, $SJ_c = 1.4$, $SJ_s = 0.44$ meV. Suplementary Figure S1 summarizes the calculated $\chi''(\omega)$ and spin wave dispersions for all three sets of parameters. From the calculation, we see that all three parameter sets give similar local susceptibilities, and therefore cannot be distinguished based on $\chi''(\omega)$ alone.

By comparing the calculated spin wave dispersion curves with data, we were able to separate which model is correct. Supplementary Figure S1b and S1c shows the outcome for the three sets of exchange couplings for the acoustic and optical modes, respectively. We see that parameters of (1) and (2) fit the acoustic and optical data slightly better. Although the imaginary part of local susceptibility and dispersion curves for different exchange parameter sets are similar, their constant energy patterns at ∼110 meV are very different, which provides key clues to the choice among different exchange coupling parameters. In the energy range around 110 meV, several optical branches are mixed together. The combined spin wave intensity patterns depend sensitively on the exchange coupling parameters. Supplementary Figure S2 compares directly the calculated patterns with the observation for the three set of exchange parameters. Supplementary Figure S2a shows the raw data, while Supplementary Figs. S2b-d plot expected scattering profiles for the three sets of parameters, respectively. Clearly, the first set of parameters describes the data much better. The second set of parameters gives scattering profiles with horizontally enhanced intensity; while the third set with $SJ_3 = 0$ overestimates the scattering intensity and gives circular shaped scattering profile.

Both models predict magnetic scattering profiles near 100 meV different from the data in Supplementary Fig. S2a. Based on these considerations, we find that the effective magnetic exchange coupling constants in the first set can best describe the data. This conclusion is further confirmed by comparing the calculated dispersion with the observed dispersion using the three sets of parameters as shown in Supplementary Figs. S2, S3 and S4.

As a remark, we note the important fact that the in-block NNN exchange J_2 must be positive (antiferromagnetic) for all candidate sets of parameters. J_2 has little effect on the first and the third branches of dispersion, but is strongly coupled to the middle branch. A ferromagnetic J_2 can push up the second branch for about 30%. This means the gap between first and second branches would be more than 40 meV, while in experiment it is clearly less than 30 meV.

Supplementary Note 4. Sum rule

Here we discuss the total moment sum rule. For a Heisenberg model with spin S, the sum rule is formulated as [34]:

$$M_o = \frac{1}{N}\sum_{\alpha}\int d\mathbf{k}\int_{-\infty}^{\infty} d\omega S^{\alpha\alpha}(\mathbf{k},\omega) = M_x + M_y + M_z = g^2\mu_B^2 S(S+1), \tag{S24}$$

where g is the Lande factor. For free electrons $g = 2$. In $Rb_{0.89}Fe_{1.58}Se_2$, the maximum possible spin $S = 2$ is expected, which gives $M_o = 24\ \mu_B^2$/Fe.

The longitudinal part M_z comes from the static moment (elastic) and the inelastic contribution. For our system, the static moment is about 3 μ_B/ Fe [19], which contributes 9 μ_B^2/Fe. The inelastic part mainly comes from the two-magnon scattering process. The magnetization reduction can be evaluated as $\Delta S = 0.5$ from the static moment for $S = 2$. From Ref. [34], we can estimate the two-magnon spectral weight as $\Delta S(1+\Delta S)g^2\mu_B^2 \simeq 3\mu_B^2$/Fe, where the normalization factor has been chosen as 1. The spectral weight from the two-magnon process is only 1/3 of the elastic part, which is much weaker than the cuprates which has $S = 1/2$. In unpolarized neutron experiments, the two-magnon spectral weight is generally very hard to detect. We will ignore it in the following treatment.

The transverse part $M_x + M_y$ mainly comes from the one-magnon spin wave spectrum. According to Eq. (1) in Ref. [33], we can get the dynamic structure factor $S(E)$ by removing the magnetic form factor. Then using Eq. (5) in Ref. [33], we can get the transverse part by integrating $S(E)$ over the whole energy range. To calculate the local dynamic susceptibility $\chi''(\omega)$ within the (H_o, K_o) scattering plane, we integrate and average the intensity in the entire Brillouin zone as marked in the red boxes of Supplementary Fig. S5. Due to the crystal symmetry, averaging the intensity in the red rectangular area will be equal to averaging the intensity all over the reciprocal space (after correcting the magnetic form factor). Different regions are chosen (1) to avoid detector gap & main beam stop where there are no signal; and (2) to reduce the influence of large-Q background which may cause an over-estimation for the magnetic intensity.

Experimentally we do not observe the neutron scattering signal above 250 meV, so we can choose the integration range from 8 to 250 for the inelastic magnetic scattering. We assume that all scattering inside the integration red box is magnetic in origin. Since single phonon cut-off is about 40 meV, we are confident that scattering we observe above 40 meV are spin waves. We get the transverse part $\sim 26 \pm 5\ \mu_B^2(f.u.)^{-1}$, where $f.u.$ means formula unit. Considering the formula of $Rb_{0.89}Fe_{1.58}Se_2$, we divide it by a factor of 1.6. The transverse part $M_x + M_y$ is evaluated as $16 \pm 3\mu_B^2/Fe$.

The total moment from our evaluation is $25 \pm 5\ \mu_B^2$/Fe, which is very close to the expected total moment from the sum rule. Thus the Heisenberg model with $S = 2$ is an appropriate description for the insulating $Rb_{0.89}Fe_{1.58}Se_2$ and the local moment spin waves describe the spin dynamics very well. We note that the errors in the local moments estimation only include statistical errors, and do not include the possible systematic errors of vanadium normalization, which can be up to 50%.